An adaptive floating node based formulation for the analysis of multiple delaminations under high cycle fatigue loading

Trabal, Guillem Gall; Bak, Brian Lau Verndal; Chen, Boyang; Carreras, Laura; Lindgaard, Esben

Published in:
Composites Part A: Applied Science and Manufacturing

DOI (link to publication from Publisher):
10.1016/j.compositesa.2022.107036

Publication date:
2022

Document Version
Publisher's PDF, also known as Version of record

Composites: Part A 160 (2022) 107036

Contents lists available at ScienceDirect

Composites Part A

journal homepage: www.elsevier.com/locate/compositesa

An adaptive floating node based formulation for the analysis of multiple delaminations under high cycle fatigue loading

Guillem Gall Trabal [a], Brian Lau Verndal Bak [a], Boyang Chen [b], Laura Carreras [a], Esben Lindgaard [a,*]

[a] Department of Materials and Production, Aalborg University, Fibigerstraede 16, DK-9220, Aalborg East, Denmark
[b] Faculty of Aerospace Engineering, Delft University of Technology, Kluyverweg 1, 2629 HS Delft, Netherlands

ARTICLE INFO

Keywords:
Fatigue
Delamination
Cohesive Zone Modeling
Floating Node Method
Adaptive refinement
Multiple delamination

ABSTRACT

A novel efficient numerical formulation for the analysis of multiple fatigue-driven delamination cracks is presented. A cohesive zone model is used in combination with an Adaptive Refinement Scheme (ARS) and an Adaptive Floating Node Method (A-FNM) element that refine the model effectively during the analysis. Novel techniques are proposed to track the positions of multiple crack tips and calculate the mode decomposed energy release rates for the individual crack tips using the J-integral. The method has been implemented in a Matlab finite element code and validated with single and multiple delamination cases with varying mode mixities. Comparisons with theoretically based predictions and available experimental data showcase the high accuracy of the method. The presented method lowers the computational time compared to standard, fully refined finite element models by a factor of 4–5.

1. Introduction

Delamination is the predominant damage mode leading to the final failure of laminated composite structures subjected to fatigue loading [1–3]. More efficient damage-tolerant designs are often disregarded due to the lack of efficient modelling tools to assess fatigue-driven delamination propagation in large-scale structures. Therefore, such predictive efficient delamination modelling tools are of high interest. Such tools would allow for more optimal designs and streamline maintenance procedures by addressing only delaminations prone to propagate.

According to [4,5], current methods to model delamination growth in laminated composite structures subjected to fatigue loading can broadly be classified into those making use of Linear Elastic Fracture Mechanics (LEFM) [6,7] and those making use of Cohesive Zone Models (CZM) [8–23]. Cohesive zone-based models are currently the preferred option due to their ability to model delamination problems with non-negligible fracture process zones, which is often the case for commonly used laminated fibrous composite materials [24–28]. Most CZMs for delamination growth under fatigue loading [8–23] are based on CZMs for quasi-static loading [29–33], where a damage mechanics variable is used to describe the stiffness degradation of the delaminating interface. Given the complex geometries and loading scenarios often present in laminated structures, CZMs are generally implemented in a Finite Element Analysis (FEA) context as Cohesive Elements (CEs). Models using CEs can be computationally demanding for large structures since it is required to have 3 to 10 cohesive elements in the Damage Process Zone (DPZ) [15,34,35]. The DPZ is only 1 to 30 mm long for most laminated composite materials [34–39] and thus several orders smaller than most structures. Furthermore, CEs need to be preallocated at all potential crack paths, which translates to all the laminate interfaces susceptible to developing delamination during the analysis [40]. The implication is that predictive simulation of fatigue-driven delamination growth in large-scale structures is computationally infeasible.

Several solutions to the mesh size problem have been proposed in the literature for quasi-static loading cases. For instance, CEs that can be larger while keeping the same level of accuracy have been formulated. In [37] this is achieved by lowering the interface strength in order to enlarge the DPZ artificially and thus allowing larger CEs to some extent [37,41,42]. However, this technique is only suitable for relatively long cracks compared to the length of the DPZ. Another approach is using adaptive integration schemes depending on the element damage status [42–45], which enables the use of larger CEs. This, however, does not solve the poor kinematic representation of the crack opening profile offered by standard CEs, limiting its effect. In [46–49] methods for enriching the displacement field in low order

* Corresponding author.
E-mail addresses: ggt@mp.aau.dk (G.G. Trabal), brianbak@mp.aau.dk (B.L.V. Bak), B.Chen-2@tudelft.nl (B. Chen), lcb@mp.aau.dk (L. Carreras), elo@mp.aau.dk (E. Lindgaard).

https://doi.org/10.1016/j.compositesa.2022.107036
Received 4 March 2022; Received in revised form 2 June 2022; Accepted 7 June 2022
Available online 16 June 2022

elements are proposed to improve the kinematic representation of the crack opening profile. Although this increases the allowable CE size, a limited improvement of the computational time is obtained [50]. The combination of high order structural elements that provide an accurate representation of the crack opening and adaptive integration has shown promising results [51]. However, even with larger elements, the preallocation of CEs at all potential crack paths alone makes delamination analysis infeasible for large multilayered laminated structures. Dynamic allocation of CEs during the analysis has been studied in the literature to eliminate the need of defining the cohesive interfaces before the analysis. This can be achieved by the use of element splitting methods such as the Phantom Node Method (PNM) [52,53] and the Extended FEM (X-FEM) method [49,54], but these are difficult to apply in multiple delamination cases. In the context of explicit dynamic analysis, modification of layered solid-shell elements to include cohesive interfaces using phantom nodes has been pursued in [55,56], while in [57] inclusion of CEs with rotational degrees of freedom in models featuring shell elements is presented. Both adaptive refinement and addition of CEs have been done using remeshing techniques [58–60] with limited reduction in computational time due to the frequent changes of the model global connectivity.

The recently developed Floating Node Method (FNM) [61], offers the possibility of applying an element-level remeshing without changing the global connectivity of the model by dividing each element into sub-elements. The FNM uses already available standard finite element formulations in its core and is simpler for multiple cohesive cracks than PNM and X-FEM. The FNM has been used to dynamically add CEs in [62–64] and to refine the area in the vicinity of a crack front in [65], where analytical DCB expressions are used to calculate a fixed-length refinement mask that moves with the crack-tip. [66] presents an adaptive refinement formulation capable of simultaneously including and refining CEs dynamically during the analysis. This is achieved by formulating a new Adaptive Refinement Scheme (ARS) that determines the cohesive zone discretisation needed along each interface, and an Adaptive FNM (A-FNM) element that can split and refine itself efficiently. The combination of the ARS and A-FNM element efficiently models complex quasi-static delamination growth scenarios in laminated composite structures featuring multiple delaminations and variable DPZ lengths. Using the FNM for analysis of delamination propagation under fatigue loading has been pursued in [67–69] using a combination of the Virtual Crack Closure Technique (VCCT) and Paris' law with the dynamic splitting of elements without further refinement.

Fatigue models for fatigue-driven delamination may be divided into hysteresis fatigue models [8–13] where every load cycle is modelled, and envelope load fatigue models [14–19] where only the maximum and sometimes minimum load of a cyclically varying load spectra are modelled. The envelope load models are preferred for high-cycle fatigue simulation because they are more computationally efficient. Among the envelope load fatigue models [14–19,19] produces the most accurate results [70] without the need of fitting parameters. It has also been recently extended to 3D applications [22,71,72] and validated against an experimental benchmark test [73,74].

In this paper, a novel 2D method for efficient analysis of high-cycle fatigue delamination propagation is presented. The formulation relies on the adaptive refinement tools presented in [66], namely the ARS and the A-FNM element, which have been coupled with the fatigue model presented in [19,22] to obtain progressive fatigue damage growth capabilities. Furthermore, the fatigue model has been extended to handle multiple delaminations simultaneously. This mainly includes a newly developed algorithm for calculating the mode decomposed energy release rates of each crack front in the model. This algorithm circumvents the problem presented in [75] for multiple crack tips propagating in opposite directions. To the knowledge of the authors, this is the first CZM based fatigue formulation with adaptive refinement and inclusion of CEs. This combination of methodologies that allows efficient analysis of complex multiple delamination scenarios in 2D constitutes the main novelty of the paper.

The article is organised as follows. A brief outline of the ARS and A-FNM element is presented in Section 2 together with the used fatigue formulation, the novel crack tracking algorithm, and the J-integral calculation for multiple delamination cracks. In Section 3 simulation results of single and multiple delamination cases are presented and discussed. Finally, Section 4 gathers the conclusions drawn from the presented work.

2. Methods

Three key methodologies are used to achieve efficient high-cycle fatigue analysis with adaptive refinement capabilities. The adaptive refinement formulation presented in [66] is used to modify the discretisation during the analysis efficiently and is briefly outlined in the following for completeness. The fatigue analysis capabilities of the A-FNM element are provided by the CZM presented in [19], which has been further developed to handle complex delamination scenarios such as multiple delaminations. Finally, new methodologies have been devised to precisely track the different crack fronts in the event of multiple delaminations.

2.1. Adaptive refinement method

The adaptive refinement capabilities in the presented formulation are effectively achieved by the Adaptive Refinement Scheme (ARS) and the Adaptive FNM based element (A-FNM) presented in [66], and summarised here for completeness. An initial coarse mesh of A-FNM elements is used to discretise the structure, as shown in Fig. 1a, with a single element through the thickness of the laminate. The ARS algorithm identifies the discretisation needs for each crack front associated traction profile using only the damage state variable D^k and the coarse refinement expected distance l_{cor} user input displayed in Fig. 1b. Then, the ARS provides each A-FNM element interface with a discretisation state: (1) Full damage state, (2) Refined state, (3) Coarse state and, (4) Idle state as shown in Fig. 1a. Each interface state corresponds to a different interface discretisation in the A-FNM element as shown in Fig. 2. Using the damage state variable D^k, which defines the DPZ, permits tracking the DPZ length changes, thus varying the refinement length accordingly without further user input. Remark that the A-FNM element interface immediately neighbouring the crack tip is set to a refined state, as seen in Fig. 1. This ensures proper discretisation of the high gradient zone between the DPZ and the start of l_{cor}. As demonstrated in [66] the l_{cor} user input (shown in Fig. 1a) can be chosen conservatively large with nearly no impact on the computational time. In case of doubt, a large value for l_{cor} should be chosen to ensure the representation of the tractions far from the DPZ.

The A-FNM element is capable of splitting, refining and coarsening itself following the element interface state information from the ARS using the FNM [61]. Each A-FNM element is initialised with four real nodes and a set of FNs which do not have an initial position assigned following [61], i.e. they are floating. To maintain global connectivity, the FNs are permanently assigned to specific A-FNM elements at the beginning of the analysis. As displayed in Fig. 2, internal FNs are connected to a single A-FNM element and can be positioned at any place in the element when needed. The Edge FNs are connected to two neighbouring A-FNM elements and are positioned on the shared edge. The A-FNM element can be partitioned or refined, creating internal sub-elements (SEs) by activating and deactivating the necessary FNs, creating different configurations as shown in Fig. 2. The number of cohesive sub-elements created along the horizontal direction in the refined configuration is based on a user-defined cohesive sub-element length l_{coh}. When an FN is activated, position and displacements are assigned to the FN using linear interpolation between real nodes or already active FNs [66]. Each newly activated FN is also connected to

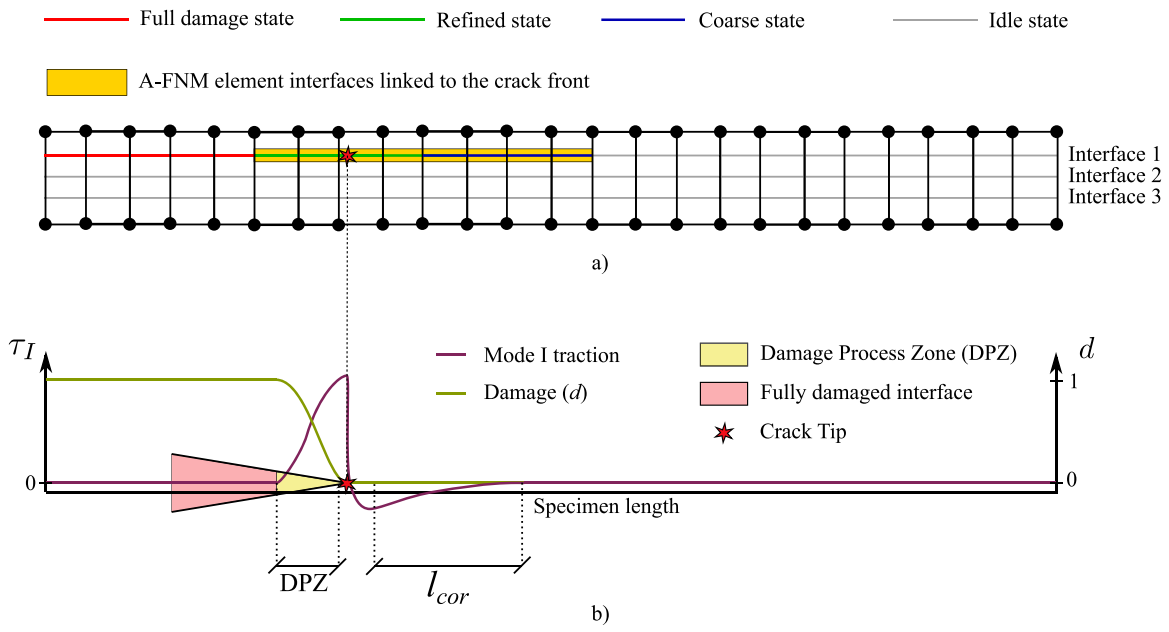

Fig. 1. (a) The discretisation resulting from applying the ARS algorithm to the above traction profile. (b) Representation of a Mode I profile with the DPZ and l_{cor} length represented.

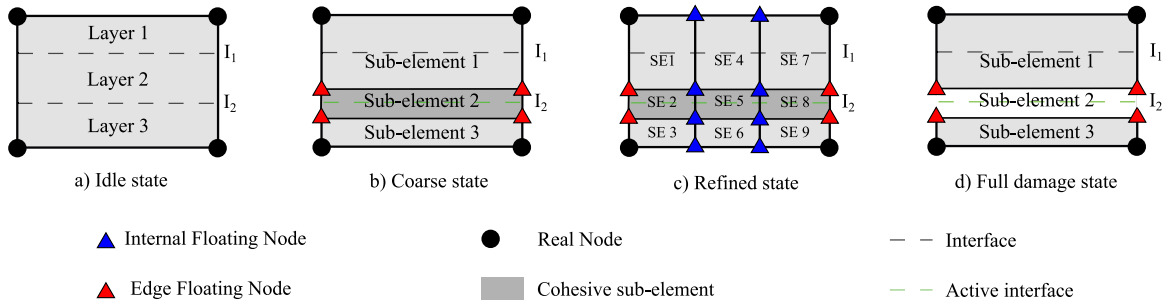

Fig. 2. The four configurations the A-FNM element can take for a single active interface.

the necessary SEs, creating an element-level connectivity that does not modify the global connectivity of the model. FNs no longer needed are deactivated, effectively coarsening the A-FNM element.

Calculation of the A-FNM element tangent stiffness matrix is performed by assembling the SE tangent stiffness matrices calculated with standard FE subroutines. The solid SEs are 4-node 2D linear layered plane strain formulation stabilised with Enhanced Assumed Strains (EAS4) [66] which prevents shear locking and enables the use of larger elements in unrefined areas. The EAS enhancement is disabled in refined areas to avoid problems derived from large aspect ratios. Cohesive SEs use a cohesive formulation that is further developed from [19,33] to model general delamination scenarios, including multiple delaminations.

2.2. The fatigue method

The fatigue formulation follows the work from [19] and is summarised here, outlining the necessary modifications to model complex multiple delamination scenarios. The fatigue model follows an envelope load approach and discretisation of the number of cycles N into cycle jumps ΔN (Fig. 3). The damage evolution is calculated for each cycle jump ΔN by integrating the current damage growth rate dD^e/dN. D^e is an energy-based damage variable uniquely related to the stiffness damage variable D^k. The model introduced in [19] presents a link between the local damage growth rate dD^e/dN and the experimentally obtained crack growth rate da/dN model without using any additional fitting parameters.

The fatigue model in [19] takes point of departure on the quasi-static CZM from [33], which is also used for the quasi-static loading phase prior to a fatigue loading block shown in Fig. 3b. The kinematics and damage law used by the CZM are shown in Fig. 4. Displacements are transformed to a mid-surface local coordinate system and split into normal (δ_2) and shearing (δ_1) components (Fig. 4a). Mode dependency of the critical energy release rate G_c and onset traction μ_0 is achieved through the Benzeggagh–Kenane criterion [33,76]. The equations governing the quasi-static CZM are listed in Table 1 where G_{Ic}, G_{IIc} and η are material parameters. One of the onset traction values, τ_{I0}, τ_{II0} is a material parameter while the remaining one is calculated through the relation $\tau_{II0} = \tau_{I0}\sqrt{G_{IIc}/G_{Ic}}$ for energy consistency [77].

The relation between the crack growth rate da/dN and the local damage rate dD^e/dN derived in [19] relies on three main assumptions: (1) The crack growth rate is a function of the load amplitude, mean load and energy release rate-based mode mixity, (2) The tractions always follow the quasi-static cohesive law as long as the interface is not fully damaged, and (3) self-similar crack growth. An example of a pure mode I analysis is shown in Fig. 3 focusing on the damage evolution of the points marked with a star and a circle. Firstly, a quasi-static loading step is applied using the quasi-static CZM formulation [19,33] (Fig. 3b). The shift to fatigue loading is done conserving the traction profile and displacement jumps (Fig. 3c). A full damage criterion is used, which brings the damage value D^e to a full damage state of 1 when the total

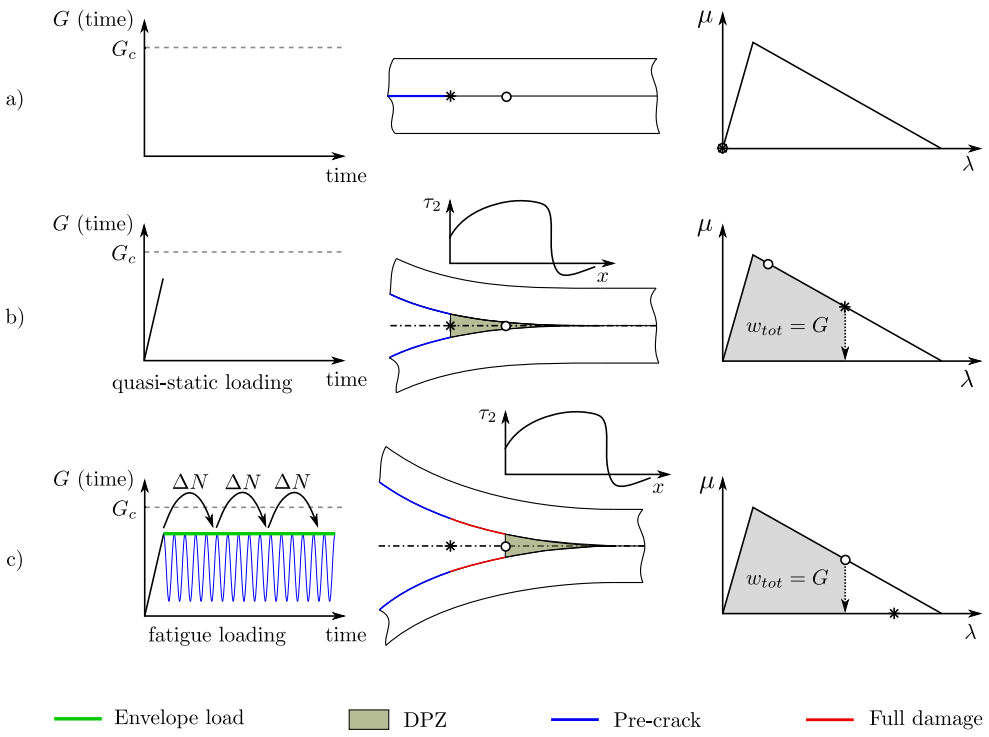

Fig. 3. Fatigue analysis sequence for a pure mode I crack: (a) Unloaded structure, (b) Quasi-static loading, (c) Fatigue loading following the envelope load approach. Notice that the traction profile is maintained in the transition between the quasi-static and fatigue loadings.

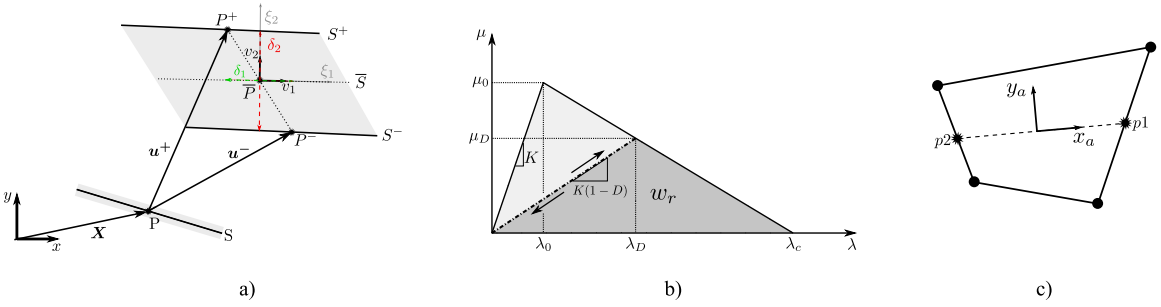

Fig. 4. (a) Kinematics of the 2D cohesive zone model. (b) Bilinear damage law used in the cohesive zone model [19,33]. (c) Local cohesive element crack tip oriented coordinate system.

Table 1
Expressions governing the CZM developed in [33] and used in [19], which applies the traction–separation law shown in Fig. 4b.

Separation norm	$\lambda = \sqrt{\langle\delta_I\rangle^2 + (\delta_s)^2}$	(1)	Normal separation	$\delta_I = \frac{1}{2}(\delta_2 + \lvert\delta_2\rvert)$	(2)
Shearing separation	$\delta_s = \lvert\delta_1\rvert$	(3)	Traction norm	$\mu = (1 - D^k)K\lambda$	(4)
Local separation-based mode mixity	$\beta = \frac{\delta_s}{\delta_I + \delta_s}$	(5)	Onset separation	$\lambda_0 = \frac{\mu_0}{K}$	(6)
Critical separation norm	$\lambda_c = \frac{2G_c}{\mu_0}$	(7)	Critical energy release rate	$G_c = G_{Ic} + (G_{IIc} - G_{Ic})B^\eta$	(8)
Current damage separation	$\lambda_D = \frac{\lambda_0\lambda_c}{\lambda_c - D^k(\lambda_c - \lambda_0)}$	(9)	Local energy mode mixity ratio	$B = \frac{\beta^2}{\beta^2 - 2\beta + 1}$	(10)
Onset traction	$\mu_0 = \sqrt{\langle\tau_{I0}\rangle^2 + [(\tau_{II0})^2 - (\tau_{I0})^2]B^\eta}$	(11)	Damage irreversibility	$D^k = \min\left(\max\left(0, \frac{\lambda_c(\lambda - \lambda_0)}{\lambda(\lambda_c - \lambda_0)}\right), 1\right)$	(12)

specific work of the cohesive tractions w_{tot} is equal to the energy release rate G [19]:

$$D^e = 1 \quad \text{if} \quad w_{tot} > G \quad \text{where} \quad w_{tot} = \int_0^{\lambda_D} \mu d\lambda \tag{13}$$

The fatigue damage model makes use of an energy-based damage variable D^e that is related to the stiffness damage variable D^k by:

$$D^e = 1 - \frac{\lambda_c(1 - D^k)K\lambda_D}{2G_c} \quad \text{for} \quad \lambda_D \geq \lambda_0 \tag{14}$$

Table 2
Partial derivatives use to obtain the relation between da/dN and dD^e/dN [19].

$\frac{\partial D^e}{\partial w_r} = -\frac{1}{G_c}$	$\frac{\partial \mu_0}{\partial B} = \frac{\eta(\tau_{II0}^2 - \tau_{I0}^2)B^{\eta-1}}{2\mu_0}$	$\frac{\partial w_r}{\partial \lambda} = \frac{K\lambda_0 - \lambda_c}{2(\lambda_0 - \lambda_c)}$
$\frac{\partial \lambda_c}{\partial G_c} = \frac{2}{\mu_0}$	$\frac{\partial w_r}{\partial \lambda_0} = \frac{K(\lambda_c - \lambda)\lambda_c^2}{2(\lambda_c - \lambda_0)}$	$\frac{\partial D^e}{\partial G_c} = \frac{w_r}{(G_c)^2}$
$\frac{\partial \lambda_0}{\partial \mu_0} = \frac{1}{K}$	$\frac{\partial G_c}{\partial B} = \eta(G_{IIc} - G_{Ic})B^{\eta-1}$	$\frac{\partial w_r}{\partial \lambda_c} = \frac{K\lambda_0(\lambda\lambda_0 + \lambda_c^2 - 2\lambda_c\lambda_0)}{2(\lambda_c - \lambda_0)}$
$\frac{\partial B}{\partial \beta} = 2B(\beta - B(2\beta - 1))\beta^{-2}$	$\frac{\partial \lambda_c}{\partial \mu_0} = \frac{-2G_c}{(\mu_0)^2}$	

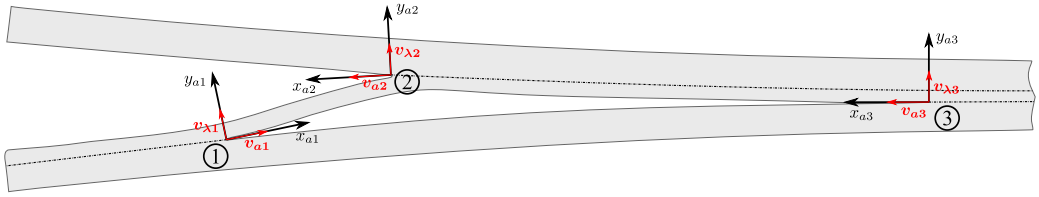

Fig. 5. A DCB-like specimen with three crack fronts and their respective local coordinate systems for the calculation of the element slopes.

The remaining ability to do non-conservative work per area unit ω_r can be determined as:

$$w_r = \frac{K\lambda_0\lambda_c(\lambda_c - \lambda)}{2(\lambda_c - \lambda_0)} \tag{15}$$

The damage rate dDe/dN is given as:

$$\begin{aligned}\frac{dD^e}{dN} =& \left(\left[\left(\left(\frac{\partial w_r}{\partial \lambda_0}\frac{\partial \lambda_0}{\partial \mu_0} + \frac{\partial w_r}{\partial \lambda_c}\frac{\partial \lambda_c}{\partial \mu_0} \right)\frac{\partial D^e}{\partial w_r}\frac{\partial \mu_0}{\partial B} \right.\right.\right. \\ &+ \left.\left.\left(\frac{\partial D^e}{\partial w_r}\frac{\partial w_r}{\partial \lambda_c}\frac{\partial \lambda_c}{\partial G_c} + \frac{\partial D^e}{\partial G_c} \right)\frac{\partial G_c}{\partial B} \right)\frac{\partial B}{\partial \beta} \right] \frac{\partial \beta}{\partial a} \\ &+ \left[\frac{\partial D^e}{\partial w_r}\frac{\partial w_r}{\partial \lambda} \right]\frac{\partial \lambda}{\partial a} \Bigg) \frac{da}{dN} = \left(F_\beta \frac{\partial \beta}{\partial a} + F_\lambda \frac{\partial \lambda}{\partial a} \right)\frac{da}{dN} \\ &\text{for} \quad \lambda \in]\lambda_0, \lambda_c[\quad \text{and} \quad D^e \in [0, 1[\end{aligned} \tag{16}$$

where the crack growth rate da/dN is obtained from a Paris' law like expression. All the partial derivatives related to the cohesive law are listed in Table 2.

The derivatives in Table 2 are only dependent on the parameters of the quasi-static cohesive law that are independent of the crack propagation direction. Although the derivatives $\partial\lambda/\partial a$ and $\partial\beta/\partial a$, are also independent on the crack growth direction, they are calculated in [19] using the assumption of self-similar crack growth, leading to the definition of the slopes $\partial\lambda/\partial x$ and $\partial\beta/\partial x$. A dependency on the crack growth direction is created when using the structural x coordinate instead of the crack growth coordinate a. In order to address this issue and obtain a general formulation, a local crack front coordinate system (x_a, y_a) is used:

$$\frac{\partial \lambda}{\partial a} = \frac{\partial \lambda}{\partial x_a} \qquad \frac{\partial \beta}{\partial a} = \frac{\partial \beta}{\partial x_a} \tag{17}$$

The coordinate system (x_a, y_a), shown in Fig. 5, is always positioned at the current crack tip location, defined as the point of damage onset, for every crack in the structure with the base vectors $\boldsymbol{v_a}$ and $\boldsymbol{v_\lambda}$ which are defined as:

$$\boldsymbol{v_a} = \boldsymbol{v_1}\frac{dD^e/d\xi_1}{\|dD^e/d\xi_1\|} \qquad \boldsymbol{v_\lambda} = \boldsymbol{v_2} \tag{18}$$

where ξ_1 is the element isoparametric horizontal coordinate, v_1 and v_2 are defined in Fig. 4a, and $\boldsymbol{v_a}$ can be understood as the Growth Driving Direction(GDD) presented in [71] applied to 2D. Notice that using Eq. (18) the vector $\boldsymbol{v_a}$ is consistently oriented on the opposite direction of the crack growth. This consistent definition of the (x_a, y_a) coordinate systems is crucial as it defines the sign of $d\lambda/da$ and $d\beta/da$, and consequently the signs of F_λ and F_β in Eq. (16). The combined static and fatigue damage formulation are applied to a 4-noded 2D linear cohesive sub-element and integrated into the A-FNM element. Therefore, $\partial\lambda/\partial x$ and $\partial\beta/\partial a$ can be calculated as proposed in [19], but using the local crack front coordinate system:

$$\frac{\partial \lambda}{\partial x_a} = \begin{cases} \frac{\delta_I}{\lambda}\frac{\partial \delta_2}{\partial x_a} + \frac{\delta_s}{\lambda}\frac{\partial \delta_1}{\partial x_a}, & \text{if } \delta_2 > 0 \\ \frac{\delta_s}{\lambda}\frac{\partial \delta_1}{\partial x_a}, & \text{if } \delta_2 \le 0 \end{cases} \tag{19}$$

$$\frac{\partial \beta}{\partial x_a} = \begin{cases} \frac{\delta_I}{(\delta_s + \delta_I)^2}\frac{\partial \delta_1}{\partial x_a} - \frac{\delta}{(\delta_s + \delta_I)^2}\frac{\partial \delta_2}{\partial x_a}, & \text{if } \delta_2 > 0 \\ 0, & \text{if } \delta_2 \le 0 \end{cases} \tag{20}$$

where the partial derivatives $\partial\delta_2/\partial x_a$ and $\partial\delta_1/\partial x_a$ can be calculated for a linearly interpolated element as [19]:

$$\frac{\partial \delta_2}{\partial x_a} = \frac{\delta_{2p2} - \delta_{2p1}}{L_e} \qquad \frac{\partial \delta_1}{\partial x_a} = \frac{\delta_{1p2} - \delta_{1p1}}{L_e} \tag{21}$$

where the points $p1$ and $p2$ are consistently defined in the local (x_a, y_a) coordinate system as shown in Fig. 4c.

Integration of the damage rate dD^e/dN obtained using Eq. (16) is performed for a given cycle jump ΔN to obtain the new damage state using a trapezoidal integration rule [19]:

$$\begin{aligned} D^e(N_n + \Delta N) &= D^e(N_n) + \int_{N_n}^{N_n+\Delta N} \frac{dD_f^e}{dN} dN + \Delta D_s^e \\ &\approx D^e(N_n) + \frac{1}{2}\left(\left.\frac{dD_f^e}{dN}\right|_{N_n} + \left.\frac{dD_f^e}{dN}\right|_{N_n+\Delta N} \right)\Delta N + \Delta D_s^e \end{aligned} \tag{22}$$

where the term ΔD_s^e is a quasi-static damage growth term, which is calculated after the application of the fatigue damage growth. This term may originate from the violation of the self-similar crack-growth assumption in coarse meshes [19] or, in the case of complex multiple delamination analysis such as the ones considered in this work, due to actual quasi-static delamination growth produced by a change in the local crack loading conditions. It is important to remark, that for single crack fatigue analysis with a monotonic decrease of the energy release rate G, the only source of quasi-static damage is the violation of self-similar crack growth for coarse meshes, which introduces a difference between the derivatives $\partial\lambda/\partial a$ and $\partial\beta/\partial a$, and the slopes $\partial\lambda/\partial x$ and $\partial\beta/\partial x$ used in the fatigue model. For further details on this issue, the reader is referred to [19]. An Adaptive Cycle Integration (ACI) technique described in [19] can be used to correct the error produced by non-self similar crack growth by assuming that the ΔD_s^e term is entirely produced by the violation of the self-similar crack growth assumption. The ACI corrects the next cycle jump ΔN to compensate for such error. A 2 point Newton–Cotes integration rule is used to calculate the cohesive sub-element tangent stiffness matrix with integration points located at the nodal positions.

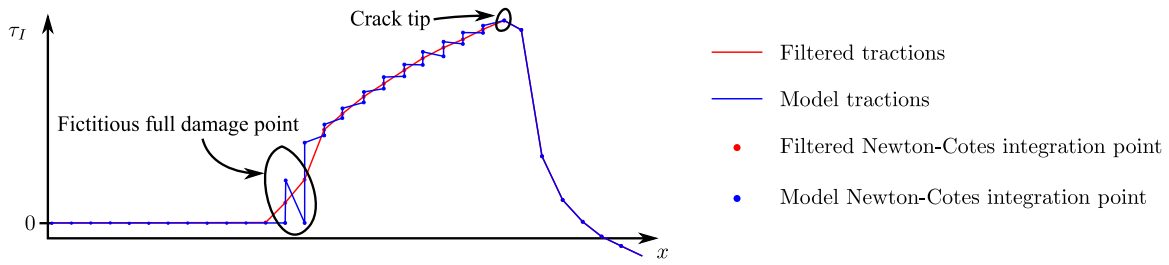

Fig. 6. Mode I traction profile before the filtering (blue) and after the filtering (red).

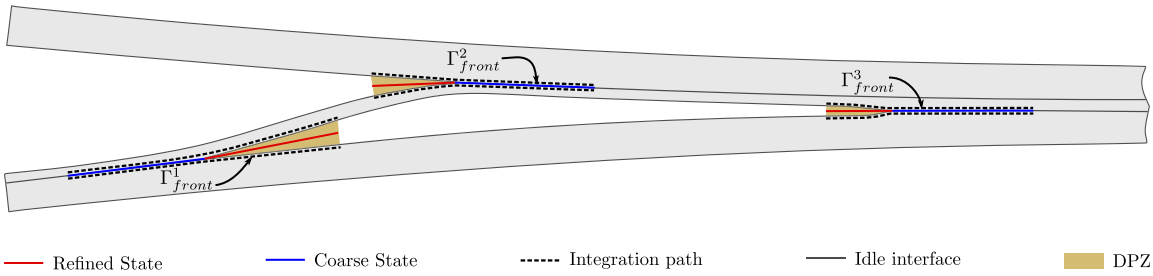

Fig. 7. Integration paths for a DCB specimen with three simultaneous delaminations. In red and blue, the refinement states determined by the ARS.

2.3. Implementation of the adaptive framework

The implementation of the cohesive fatigue formulation from Section 2.2 within the adaptive formulation requires the development of an algorithm that tracks the crack fronts accurately providing them with the correct local crack tip coordinate system, the individual crack front energy release rate G, and a crack growth rate da/dN. The calculation of the aforementioned quantities is done at each iteration to allow large changes in the energy release rate and mode mixity at each crack tip during each of the cycle jumps ΔN, which enables the method for complex delamination scenarios compared to [19].

The crack front tracking is done based on the damage state of the structure. In CZM related literature, the crack tip is either defined as the point of damage onset or the point at which full damage is achieved. For the calculations presented in this work, the crack tip is defined as the location of damage onset. The position at which the transition between full damage state $d = 1$ and undamaged or partial damage state $1 > d \geq 0$ occurs is referred to as the full damage point. Remark that each crack front will contain a crack tip and a full damage point. In order to calculate the partial derivatives in Eq. (16) and mode decomposed energy release rates G_I and G_{II}, the full damage point needs to be located. The damage rate dD^e/dN in Eq. (16) is based on an expression containing first-order derivatives of displacement-based quantities (element slopes), which are element piece-wise constant. Because of that, the damage evolution is not identical for overlapping Newton–Cotes integration points creating the zig-zagging traction profile shown in Fig. 6. When applying the full damage criterion in Eq. (13) to a couple of overlapping integration points, one integration point may become fully damaged while the other one does not. With the definition of the full damage point outlined above, a fictitious full damage point might appear, which needs to be resolved (Fig. 6). In order to consistently locate the full damage point before applying the ARS, an averaging of the damage value on the coincident integration points and elimination of the fictitious full damage points is performed, which creates a filtered traction profile shown in Fig. 6. The filtered tractions are only used for identification of the full damage point and crack tip location without overwriting the true damage values and thus remains energetically consistent. The calculation of the $J-$Integral is performed using the unmodified original traction profile. Note that the resolution of the crack tip tracking algorithm is the length of one cohesive sub-element as the crack tip is always located at a Newton–Cotes integration point.

The refining and coarsening of the A-FNM elements constantly creates and eliminates cohesive sub-elements that need to be linked with a crack front and its fatigue-related quantities (G, da/dN and crack front local coordinate system). The A-FNM element interfaces are assigned a crack front using the state provided by the ARS algorithm. Each A-FNM element interface containing a crack tip and its neighbouring A-FNM element interfaces with a Refined or Coarse state are assigned to that single crack front (Fig. 1a). This approach is not applicable in the case of crack coalescence in the same interface, which is also not covered by the fatigue model from [19], because the mode decomposed $J-$Integral cannot decouple the energy release rate G associated with each coalescing crack front [72,78].

The calculation of the crack growth rate da/dN is done by applying a Paris' law-like expression, which requires the calculation of the mode decomposed energy release rates G_I and G_{II} as done in [19,22]. The path independent mode decomposed $J-$Integral [78] is used to calculate G_I and G_{II} for each crack front in the model:

$$J^i_{front} = J^{i,I}_{front} + J^{i,II}_{front} = G = \left(- \int_{\Gamma^i_{front}} \tau_{11} \frac{\partial \delta_2}{\partial x^i_a} dx^i_a \right) + \left(- \int_{\Gamma^i_{front}} \tau_2 \frac{\partial \delta_1}{\partial x^i_a} dx^i_a \right) \tag{23}$$

where the path independence property is used to define the Γ^i_{front} path containing only the cohesive interface for each crack front as shown in Fig. 7. The derivatives $\frac{\partial \delta_1}{\partial x_a}$ and $\frac{\partial \delta_2}{\partial x_a}$ are calculated using Eq. (21). The calculation of the number of cycles ΔN_i for the i_{th} cycle jump is calculated as:

$$\Delta N = \frac{\Delta a_t}{max(da_i/dN)} \tag{24}$$

where Δa_t is a user-selected crack growth target per cycle jump, and $max(da_i/dN)$ is the maximum crack growth rate of all the crack fronts. Therefore, ΔN is based only on the fastest propagating crack tip. This approach is similar to what is proposed in [22] for a 3D delamination front with different crack growth rates along a single continuous curved crack front. As suggested in [19], an adaptive procedure to vary ΔN is used in case of non-convergence for a given cycle jump, increasing or decreasing its value sequentially until convergence is reached.

ANSYS Mechanical 2020 R2 is used for the definition of the geometry, boundary conditions (BCs), material properties, layup and mesh.

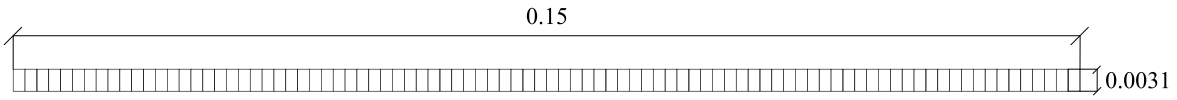

(a) Initial coarse A-FNM element mesh used in all the numerical simulations.

(b) Standard FEA mesh used to asses the performance of the adaptive formulation.

Fig. 8. Specimen and meshes used for the (a) adaptive and (b) standard numerical simulations.

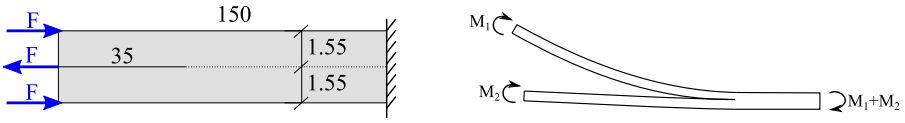

Fig. 9. On the left, boundary conditions to model the moment loaded DCB specimen (right) in the FE analysis.

The adaptive fatigue formulation, including the ARS and the A-FNM element incorporating the fatigue model presented in Section 2, has been implemented in an FEA Matlab code. The addition of pre-cracks, the adaptive refinement parameters, and fatigue properties is done in an additional pre-processing step in Matlab.

3. Results

Two sets of results are presented in this section. Firstly, the verification of the implementation for single delamination cases, which can be easily compared to theoretical obtained solutions, and available experimental data is presented. Secondly, multiple delamination analyses to validate the model's capabilities, namely the modelling of complex multiple delamination scenarios, are presented. The performance of the adaptive fatigue formulation is compared to a Matlab implementation using the same underlying formulations (EAS4 and the cohesive fatigue model) without the adaptive capabilities and an equivalent fully refined mesh. All the numerical simulations have been performed with the same basic specimen and A-FNM element coarse mesh shown in Fig. 8(a) with the material properties shown in Table 3 and the following Paris' law:

$$\frac{da}{dN} = \begin{cases} C\left(\frac{G}{G_c}\right)^m & \text{for} \quad G_{th}(\Phi) < G < G_c(\Phi) \\ 0 & \text{for} \quad G \leq G_{th}(\Phi) \end{cases} \tag{25}$$

where G_{th} is the fatigue crack growth threshold and the parameters m and C are mode dependent [79]:

$$m = \Phi^2(m_{II} - m_I - m_m) + \Phi m_m + m_I \tag{26}$$

$$\log C = \Phi^2 \log\left(\frac{C_{II}}{C_m C_I}\right) + \Phi \log(C_m) + \log(C_I) \tag{27}$$

$$\Phi = \frac{G_{II}}{G_{II} + G_I} \tag{28}$$

The A-FNM element length, cohesive element length l_{coh}, and the length of the coarse refined zone l_{cor} for each case are listed in Table 4. A crack growth target (Δa_t) of 1 cohesive sub-element is used in all the simulations.

A comparison between the numerical model and the theoretically predicted crack tip position is presented in the multiple delaminations results. The theoretical prediction of the crack length a_m after m cycle jumps is done by numerical integration of Eq. (25) [19]:

$$a_m = a_0 + \frac{1}{2}\sum_i^m \left(\left.\frac{da}{dN}\right|_{N_i} + \left.\frac{da}{dN}\right|_{N_{i+1}}\right) \Delta N_i \tag{29}$$

where a_0 is the initial pre-crack length. Remark that the model crack tip tracking algorithm has a resolution of the length of a cohesive sub-element.

Table 3
Material properties used for the analyses [15,19,80].

Material properties			Interface properties			Fatigue properties		
E_{11}	120	[GPa]	G_{Ic}	260	[N/m]	C_I	3.08e−3	[mm/cycle]
$E_{22} = E_{33}$	10.5	[GPa]	G_{IIc}	1002	[N/m]	C_{II}	1.49e−1	[mm/cycle]
$G_{12} = G_{13}$	5.3	[GPa]	τ_{I0}	30	[MPa]	C_m	458 087	[mm/cycle]
G_{23}	3.5	[GPa]	τ_{II0}	60	[MPa]	m_I	5.4	[–]
$\nu_{12} = \nu_{13}$	0.3	[–]	η	2.73	[–]	m_{II}	4.5	[–]
ν_{23}	0.51	[–]	K	30e6	[N/mm^3]	m_m	4.94	[-]

Table 4
Mesh parameters and ARS l_{cor} parameter used in the DCB, ENF and MMB numerical simulations.

Parameter [mm]	DCB/MMB	ENF	Mult.
Cohesive elem. length l_{coh}	0.119	2.38	0.208
A-FNM elem. length	1.66	1.66	1.66
ARS l_{cor} parameter	6.66	6.66	6.66

3.1. Single delamination verification

A set of moment controlled fatigue numerical simulations are performed with the specimen and BCs shown in Fig. 9, varying M_1 and M_2 to obtain a pure mode I, pure mode II and mixed-mode (Φ = 0.5) loading conditions [81]. The moment loaded DCB simulations feature a constant energy release rate G during the fatigue induced delamination growth allowing for a direct comparison to the theoretical Paris' law. A standard Newton–Raphson solver with force control was used because the sub-critical delamination growth does not feature a softening response. As shown in Fig. 10 the presented adaptive fatigue formulation can accurately reproduce the theoretical Paris' law for a ratio of G/G_c in the range 0.2–0.9. Fig. 11 shows that the energy release rate is kept at a constant level as the adaptive refinement dictated by the ARS is applied throughout the analysis.

DCB, ENF and MMB displacement controlled simulations (Fig. 12) are also simulated to prove the ability of the adaptive refinement formulation to demonstrate that the method can handle the variation in the length of the DPZ produced by the decrease in the energy release rate G. A standard Newton–Raphson solver with displacement control is used for the DCB, ENF and MMB analyses. The instantaneous crack growth rate da/dN_n for a cycle jump n is calculated in a post-processing phase after the analysis as $da/dN_n = (a_{n+1} - a_{n-1})/(N_{n+1} - N_{n-1})$. This procedure filters out sharp variations on the instantaneous calculation of da/dN that appear when the crack front does not propagate an entire element as expected by the crack growth target value of 1 cohesive sub-element. Some degree of scattering in the extracted da/dN from the model is still expected. Accurate results compared to the theoretical Paris' law are obtained in the three cases Fig. 13. Remark that the

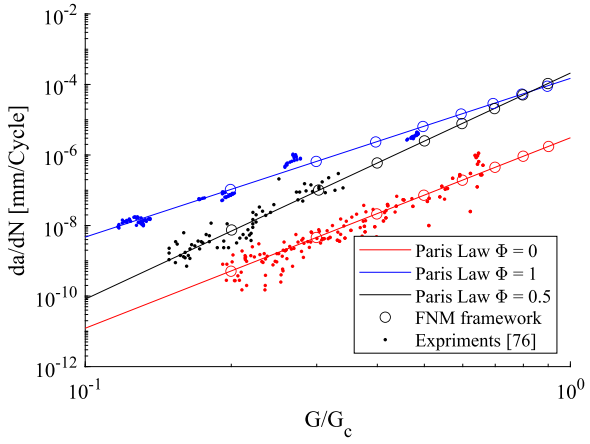

Fig. 10. Comparison between the theoretical Paris' law, the results in the model for the moment loaded specimens and the experimental results from [82].

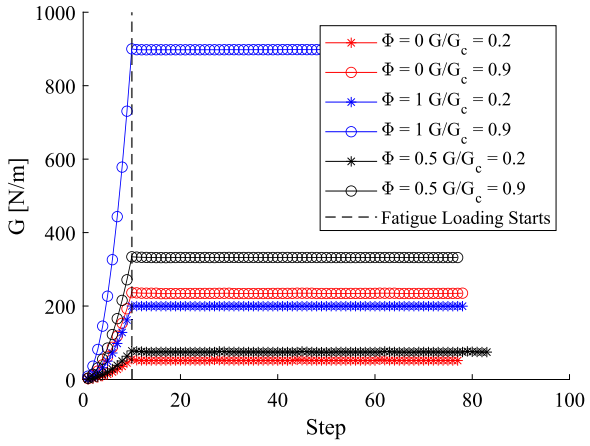

Fig. 11. Values of the energy release rate G evolution of selected moment loaded DCB analyses.

Table 5
Comparison of the computational performance between the reference and the adaptive formulation.

CPU time [s]	DCB	ENF	MMB
Reference	4301	1523	10 783
A-FNM	792	311	2545
Speed-up	5.42	4.88	4.23

aforementioned scatter observed in Fig. 13 has also been observed in the fully refined standard FE model and in [22]. The final deformed mesh at the end of the analysis displaying the state of the refinement is shown in Fig. 14.

The computational time improvement when using the adaptive fatigue formulation is shown in Table 5 where the performance in terms of computational time is improved by a factor of 4–5 compared to the reference model. For each presented case, the average of the CPU time spent for the solution of 5 analyses is computed and reported. The CPU time is not affected by any Matlab internal parallelisation process. The fully refined reference model uses the same fatigue formulation and solid EAS4 elements as the adaptive formulation with the mesh shown in Fig. 8(b). An increase of the computational gain for larger structures as the increase in DOFs is higher for a fully refined model than for the adaptive refinement formulation. For instance, a computational speed-up factor of around 100 is obtained when analysing a specimen with a length of 1.2 m and having identical conditions as the DCB displacement controlled simulation.

3.2. Multiple delamination numerical simulations

A double delamination simulation is performed with the specimen and BCs shown in Fig. 15(a) to validate that the adaptive formulation can successfully handle complex multiple delamination scenarios. The analysis is carried out under displacement controlled conditions. The proposed benchmark analysis metrics in Figs. 16(a) and 16(b) show a smooth response in the values of the mode mixity Φ and G/G_c ratio. An excellent agreement between the theoretical Paris' law solution and the results from the simulation are shown in Fig. 16(c).

The widely used triple delamination benchmark problem proposed in [83] for quasi-static delamination models is applied under fatigue loading conditions to challenge the presented adaptive fatigue framework. The specimen and boundary conditions shown in Fig. 15(b) feature three delamination fronts growing in different directions. To the knowledge of the authors, this is the first time that the benchmarking from [83] is used under fatigue loading. The material properties for the simulation are listed in Table 3 and the Paris' law from Eq. (25) is used. A standard Newton–Raphson solver with displacement control is used. The applied load spectrum is displayed on Fig. 17. The quasi-static load–displacement curve of the fatigue analysis, superposed on top of the one followed during a quasi-static analysis, is shown in Fig. 18(a), where the two fatigue loading blocks are marked. The first fatigue loading starts before the unstable propagation of the multiple delaminations represented by the abrupt vertical jump in the quasi-static response curve at a displacement value of 0.0028 m.

The fatigue response curve in Fig. 18(a) shows how the adaptive fatigue formulation can capture the propagation of the multiple delaminations, which is a phase characterised by very rapid crack growth and changing local loading conditions. After that, the second quasi-static ramping is applied, followed by the second fatigue loading block. Fig. 18(b)-c show the evolution of G and Φ for the three crack fronts during the analysis visualising the challenging local crack front conditions that change during the analysis as the crack fronts interact with each other. The deformed structure at three instants of the analysis marked in Fig. 18 as ①, ② and ③ is shown in Fig. 19.

Comparison with the predicted crack tip positions using the theoretical Paris' law is provided in Fig. 20 for the three stages of the analysis marked as A, B and C in Fig. 18(a). The theoretical Paris' law results and the simulation results are in good agreement for the first stage of the simulation (A), in which crack front interaction is low Fig. 20(a). However, minor differences between the Paris' law prediction and the model start just before the crack tip 2 starts propagating at 1500 cycles. A good agreement between the Paris' law based prediction and the simulation result is shown in Fig. 20(b)-c for stages B and C until the end of the analysis with a good degree of accuracy, given the complexity of the numerical simulation. Such difference could arise from the theoretical solution's inability to account for changes in the DPZ provoked by the changing load ratio and mode mixity.

4. Conclusion

A new formulation for efficient simulation of fatigue-driven propagation of multiple delamination cracks is presented. The formulation uses the Adaptive Refinement Scheme (ARS) and an Adaptive Floating Node Method (A-FNM) element presented in [66] to model the propagation of multiple delamination cracks efficiently. The ARS and A-FNM element combination effectively refines and coarsens the model without modifying the global connectivity. The fatigue-driven propagation of multiple crack tips is achieved by adapting the cohesive zone formulation and element presented in [19], which has been shown to provide accurate results without relying on fitting parameters. In order to model multiple delamination fronts, the fatigue model has been extended with

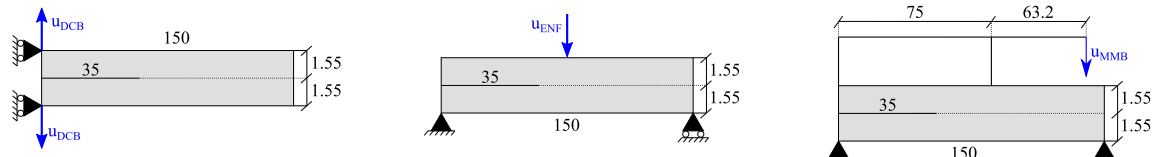

(a) DCB numerical simulation specimen and BCs.

(b) ENF numerical simulation specimen and BCs.

(c) MMB numerical specimen and BCs.

Fig. 12. Specimens and BCs for the displacement controlled single delamination DCB, ENF and MMB simulations.

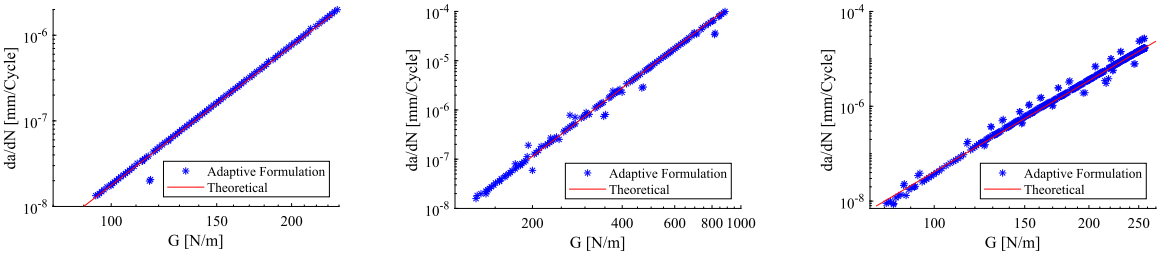

(a) DCB numerical simulation.

(b) ENF numerical simulation.

(c) MMB numerical simulation.

Fig. 13. Comparison between the theoretical Paris' law and the results obtained with the adaptive formulation for (a) DCB, (b) ENF and (c) MMB numerical simulations.

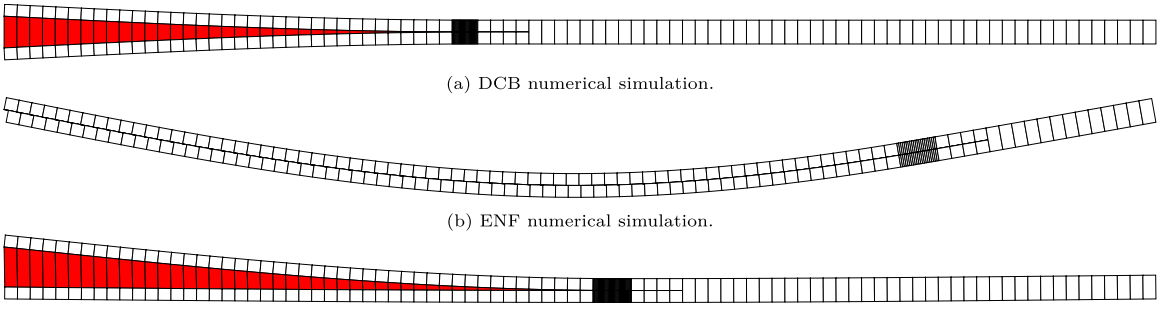

(a) DCB numerical simulation.

(b) ENF numerical simulation.

(c) MMB numerical simulation.

Fig. 14. Final deformed specimen for the DCB, ENF and MMB analyses.

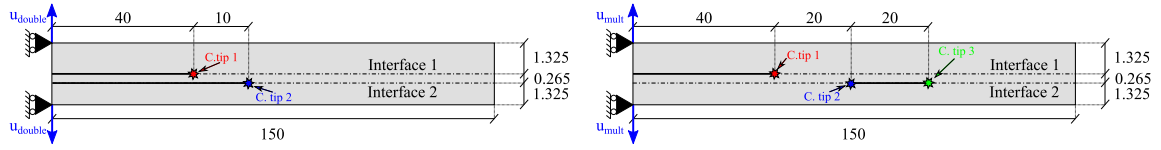

(a) Double delamination numerical simulation specimen and BCs.

(b) Triple delamination numerical simulation specimen and BCs.

Fig. 15. Double and triple delamination numerical simulation specimens and BCs.

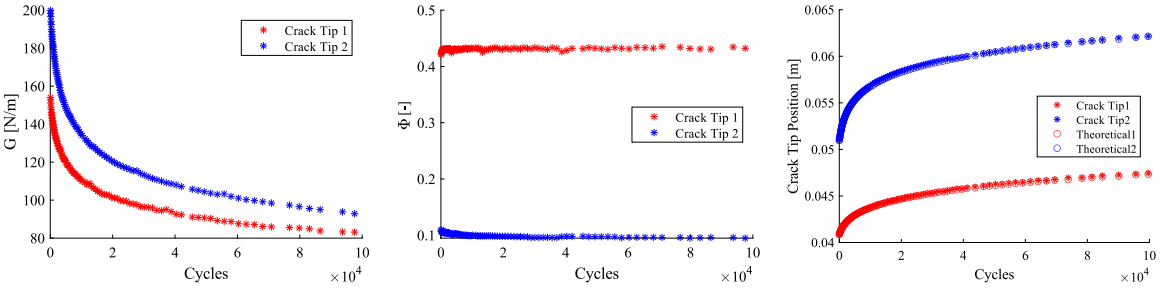

(a) Energy release rate.

(b) Energy based mode mixity Φ.

(c) Theoretical based solution comparison.

Fig. 16. (a) Energy release rate G, (b) Energy based mode mixity Φ, and (c) Comparison between the theoretical and the adaptive formulation crack growth for the double delamination numerical simulation.

methodologies that allow crack fronts to propagate simultaneously in different directions. A methodology to correctly identify each crack front and its growing direction assigning it a local coordinate system, has been devised. The energy release rate of each crack front is

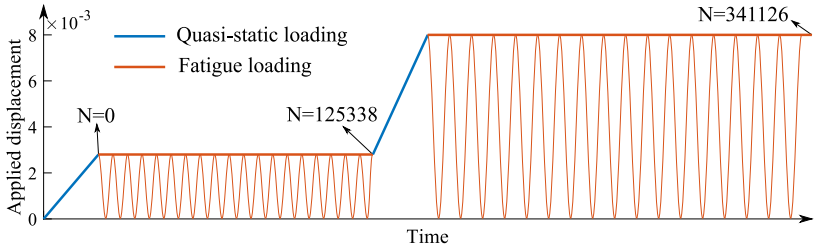

Fig. 17. Load spectra applied to the multiple delamination specimen.

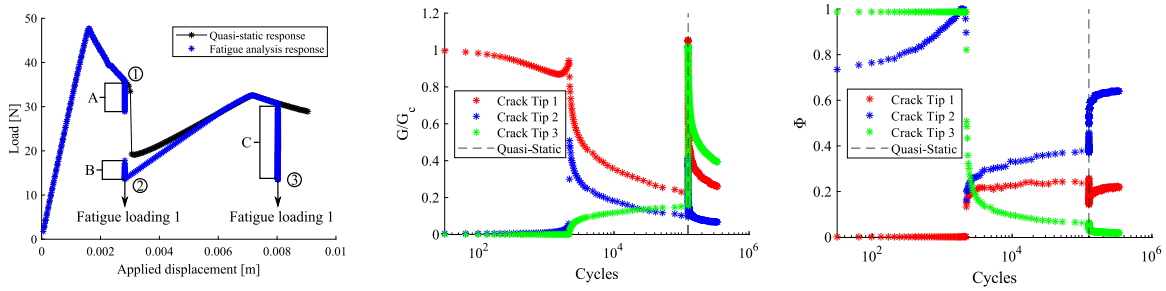

(a) Load-displacement curve. (b) Energy release rate G. (c) Energy based mode mixity Φ.

Fig. 18. (a) Load displacement response curves for quasi-static and fatigue loading, evolution of (b) Energy release rate ratio G/G_c and (c) Energy based mode mixity Φ for the triple delamination numerical simulation.

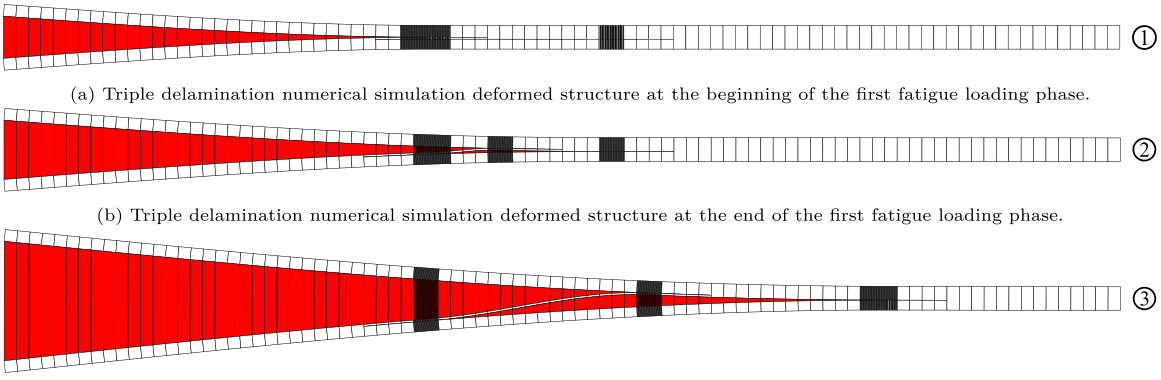

(a) Triple delamination numerical simulation deformed structure at the beginning of the first fatigue loading phase.

(b) Triple delamination numerical simulation deformed structure at the end of the first fatigue loading phase.

(c) Triple delamination numerical simulation deformed structure at the end of the second fatigue loading phase.

Fig. 19. Triple delamination numerical simulation deformed structure at three different points of the analysis.

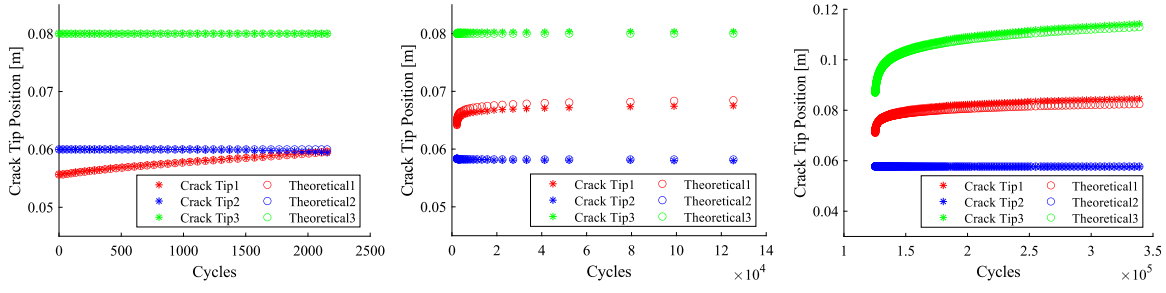

(a) Part A comparison. (b) Part B comparison. (c) Part C comparison.

Fig. 20. Comparison between the adaptive formulation results and the predicted crack tip position based on the applied Paris-law.

calculated using the J–Integral using the information provided by the ARS to determine the extension of the cohesive interface. The only necessary user inputs for the ARS and the A-FNM element are the coarse discretisation length l_{coh} and cohesive sub-element length l_{coh}.

Numerical studies of a moment loaded DCB specimen for mode I, II, and mixed-mode conditions perfectly agree with the provided Paris' law and available experimental data for a wide range of G/G_c ratios. Moreover, the steady-state constant energy release rate is still achieved even with the adaptive mesh refinement. A perfect agreement with the applied Paris' law is also achieved under displacement loaded DCB, ENF and MMB simulations with a computational factor between 4 and 5 compared to standard, fully refined FE models. It is also noticed

that speed-ups of the order of hundreds or even higher for larger FE models are expected. Two multiple delamination cases showcase the ability of the framework to capture multiple delamination crack fronts propagating in different directions with different growth rates. The well known complex multiple delamination benchmark from [83], featuring a rapid crack growth critical point, is successfully computed with the presented framework showing a good level of accuracy when compared to a theoretical Paris' law prediction. However, given the high level of complexity of the triple delamination analysis shown in [83], further fatigue experimental evidence would be desirable. The presented fatigue methodology can be used for the efficient progressive analysis of 2D multiple delaminations and to further research CZM-based fatigue propagation formulations.

CRediT authorship contribution statement

Guillem Gall Trabal: Conceptualization, Methodology, Software, Validation, Visualization, Investigation, Writing – original draft, Writing – review & editing. **Brian Lau Verndal Bak:** Supervision, Conceptualization, Methodology, Writing – review & editing, Funding acquisition. **Boyang Chen:** Supervision, Conceptualization, Methodology, Writing – review & editing. **Laura Carreras:** Supervision, Conceptualization, Methodology, Writing – review & editing. **Esben Lindgaard:** Supervision, Conceptualization, Methodology, Writing – review & editing, Funding acquisition.

Declaration of competing interest

The authors declare that they have no known competing financial interests or personal relationships that could have appeared to influence the work reported in this paper.

Data availability

Data will be made available on request.

Acknowledgements

This work is supported by the Talent Management Programme at Aalborg University, Denmark (Internal grant number: 771120). This support is gratefully acknowledged.

References

[1] Pagano N, Schoeppner G. 2.13 - Delamination of polymer matrix composites: Problems and assessment. In: Kelly A, Zweben C, editors. Comprehensive composite materials. Oxford: Pergamon; 2000, p. 433–528. http://dx.doi.org/10.1016/B0-08-042993-9/00073-5.

[2] Hallett SR, Jiang WG, Khan B, Wisnom MR. Modelling the interaction between matrix cracks and delamination damage in scaled quasi-isotropic specimens. Compos Sci Technol 2008;68(1):80–9. http://dx.doi.org/10.1016/j.compscitech.2007.05.038.

[3] Zubillaga L, Turon A, Renart J, Costa J, Linde P. An experimental study on matrix crack induced delamination in composite laminates. Compos Struct 2015;127:10–7. http://dx.doi.org/10.1016/j.compstruct.2015.02.077.

[4] Bak BLV, Sarrado C, Turon A, Costa J. Delamination under fatigue loads in composite laminates: A review on the observed phenomenology and computational methods. Appl Mech Rev 2014;66(6). http://dx.doi.org/10.1115/1.4027647.

[5] Turon A, Bak B, Lindgaard E, Sarrado C, Lund E. Interface elements for fatigue-driven delaminations in advanced composite materials. In: Camanho PP, Hallett SR, editors. Numerical modelling of failure in advanced composite materials. Woodhead publishing series in composites science and engineering, Woodhead Publishing; 2015, p. 73–91. http://dx.doi.org/10.1016/B978-0-08-100332-9.00003-7.

[6] Pradhan SC, Tay TE. Three-dimensional finite element modelling of delamination growth in notched composite laminates under compression loading. Eng Fract Mech 1998;60(2):157–71. http://dx.doi.org/10.1016/S0013-7944(98)00007-1.

[7] Krueger R. Development and application of benchmark examples for mixed-mode i/ii quasi-static delamination propagation predictions. National Aeronautics and Space Administration, Langley Research Center; 2012.

[8] Nguyen O, Repetto E, Ortiz M, Radovitzky R. A cohesive model of fatigue crack growth. Int J Fract 2001;110(4):351–69.

[9] Roe K, Siegmund T. An irreversible cohesive zone model for interface fatigue crack growth simulation. Eng Fract Mech 2003;70(2):209–32.

[10] Maiti S, Geubelle PH. A cohesive model for fatigue failure of polymers. Eng Fract Mech 2005;72(5):691–708. http://dx.doi.org/10.1016/j.engfracmech.2004.06.005.

[11] Abdul-Baqi A, Schreurs P, Geers M. Fatigue damage modeling in solder interconnects using a cohesive zone approach. Int J Solids Struct 2005;42(3):927–42. http://dx.doi.org/10.1016/j.ijsolstr.2004.07.026.

[12] Tumino D, Cappello F. Simulation of fatigue delamination growth in composites with different mode mixtures. J Compos Mater 2007;41(20):2415–41. http://dx.doi.org/10.1177/0021998307075439.

[13] Springer M, Turon A, Pettermann H. A thermo–mechanical cyclic cohesive zone model for variable amplitude loading and mixed–mode behavior. Int J Solids Struct 2019;159:257–71. http://dx.doi.org/10.1016/j.ijsolstr.2018.10.004.

[14] Robinson P, Galvanetto U, Tumino D, Bellucci G, Violeau D. Numerical simulation of fatigue-driven delamination using interface elements. Internat J Numer Methods Engrg 2005;63(13):1824–48.

[15] Turon A, Costa J, Camanho P, Dávila C. Simulation of delamination in composites under high-cycle fatigue. Composites A 2007;38(11):2270–82. http://dx.doi.org/10.1016/j.compositesa.2006.11.009, CompTest 2006.

[16] Pirondi A, Moroni F. A progressive damage model for the prediction of fatigue crack growth in bonded joints. J Adhes 2010;86(5–6):501–21. http://dx.doi.org/10.1080/00218464.2010.484305.

[17] Harper PW, Hallett SR. A fatigue degradation law for cohesive interface elements – Development and application to composite materials. Int J Fatigue 2010;32(11):1774–87. http://dx.doi.org/10.1016/j.ijfatigue.2010.04.006.

[18] Kawashita LF, Hallett SR. A crack tip tracking algorithm for cohesive interface element analysis of fatigue delamination propagation in composite materials. Int J Solids Struct 2012;49(21):2898–913. http://dx.doi.org/10.1016/j.ijsolstr.2012.03.034.

[19] Bak BLV, Turon A, Lindgaard E, Lund E. A simulation method for high-cycle fatigue-driven delamination using a cohesive zone model. Int Al J Numer Methods Eng 2015;106(3):163–91. http://dx.doi.org/10.1002/nme.5117.

[20] Tao C, Qiu J, Yao W, Ji H. A novel method for fatigue delamination simulation in composite laminates. Compos Sci Technol 2016;128:104–15.

[21] Amiri-Rad A, Mashayekhi M. A cohesive zone approach for fatigue-driven delamination analysis in composite materials. Appl Compos Mater 2017;24(4):751–69.

[22] Carreras L, Turon A, Bak BL, Lindgaard E, Renart J, Martin de la Escalera F, Essa Y. A simulation method for fatigue-driven delamination in layered structures involving non-negligible fracture process zones and arbitrarily shaped crack fronts. Composites A 2019;122(January):107–19. http://dx.doi.org/10.1016/j.compositesa.2019.04.026.

[23] Dávila CG, Rose CA, Murri GB, Jackson WC, Johnston WM. Evaluation of fatigue damage accumulation functions for delamination initiation and propagation. National Aeronautics and Space Administration, Langley Research Center; 2020.

[24] Lindgaard E, Bak BLV. Experimental characterization of delamination in off-axis GFRP laminates during mode I loading. Compos Struct 2019;220(February):953–60. http://dx.doi.org/10.1016/j.compstruct.2019.04.022.

[25] Jensen SM, Martos MJ, Bak BL, Lindgaard E. Formulation of a mixed-mode multilinear cohesive zone law in an interface finite element for modelling delamination with R-curve effects. Compos Struct 2019;216(February):477–86. http://dx.doi.org/10.1016/j.compstruct.2019.02.029.

[26] Jensen S, Martos M, Lindgaard E, Bak B. Inverse parameter identification of n-segmented multilinear cohesive laws using parametric finite element modeling. Compos Struct 2019;225:111074. http://dx.doi.org/10.1016/j.compstruct.2019.111074.

[27] Jensen SM, Bak BL, Bender JJ, Lindgaard E. Transition-behaviours in fatigue-driven delamination of GFRP laminates following step changes in block amplitude loading. Int J Fatigue 2021;144(June 2020):106045. http://dx.doi.org/10.1016/j.ijfatigue.2020.106045.

[28] Jensen S, Bak B, Bender J, Carreras L, Lindgaard E. Transient delamination growth in GFRP laminates with fibre bridging under variable amplitude loading in G-control. Composites B 2021;225:109296. http://dx.doi.org/10.1016/j.compositesb.2021.109296.

[29] Dugdale DS. Yielding of steel sheets containing slits. J Mech Phys Solids 1960;8(2):100–4.

[30] Barenblatt GI, et al. The mathematical theory of equilibrium cracks in brittle fracture. Adv Appl Mech 1962;7(1):55–129.

[31] Mi Y, Crisfield MA, Davies GAO. Progressive delamination using interface elements. J Compos Mater 1997;32(14/1998):1246–72.

[32] Camanho P, Davila C. Mixed-mode decohesion finite elements in for the simulation composite of delamination materials. Nasa 2002;TM-2002-21(June):1–37. http://dx.doi.org/10.1177/002199803034505.

[33] Turon A, Camanho P, Costa J, Dávila C. A damage model for the simulation of delamination in advanced composites under variable-mode loading. Mech Mater 2006;38(11):1072–89. http://dx.doi.org/10.1016/j.mechmat.2005.10.003.

[34] Davila C, Camanho P, de Moura M. Mixed-mode decohesion elements for analyses of progressive delamination. In: 19th AIAA applied aerodynamics conference. 2001, p. 1486.

[35] Falk ML, Needleman A, Rice JR. A critical evaluation of cohesive zone models of dynamic fracture. J Phys IV 2001;11(PR5):Pr5–43.

[36] Moës N, Belytschko T. Extended finite element method for cohesive crack growth. Eng Fract Mech 2002;69(7):813–33.

[37] Turon A, Dávila CG, Camanho PP, Costa J. An engineering solution for mesh size effects in the simulation of delamination using cohesive zone models. Eng Fract Mech 2007;74(10):1665–82. http://dx.doi.org/10.1016/j.engfracmech.2006.08.025.

[38] Harper PW, Hallett SR. Cohesive zone length in numerical simulations of composite delamination. Eng Fract Mech 2008;75(16):4774–92. http://dx.doi.org/10.1016/j.engfracmech.2008.06.004.

[39] Soto A, González E, Maimí P, Turon A, Sainz de Aja J, de la Escalera F. Cohesive zone length of orthotropic materials undergoing delamination. Eng Fract Mech 2016;159:174–88. http://dx.doi.org/10.1016/j.engfracmech.2016.03.033.

[40] Needleman A. An analysis of tensile decohesion along an interface. J Mech Phys Solids 1990;38(3):289–324. http://dx.doi.org/10.1016/0022-5096(90)90001-K.

[41] Harper PW, Sun L, Hallett SR. A study on the influence of cohesive zone interface element strength parameters on mixed mode behaviour. Composites A 2012;43(4):722–34. http://dx.doi.org/10.1016/j.compositesa.2011.12.016.

[42] Lindgaard E, Bak B, Glud J, Sjølund J, Christensen E. A user programmed cohesive zone finite element for ANSYS mechanical. Eng Fract Mech 2017;180:229–39.

[43] Remacle J, Lambrechts J, Seny B. Blossom-Quad: A non-uniform quadrilateral mesh generator using a minimum-cost perfect-matching algorithm. International 2012;89(9):1102–19. http://dx.doi.org/10.1002/nme.

[44] Do BC, Liu W, Yang QD, Su XY. Improved cohesive stress integration schemes for cohesive zone elements. Eng Fract Mech 2013;107:14–28. http://dx.doi.org/10.1016/j.engfracmech.2013.04.009.

[45] Bak BL, Lindgaard E, Lund E. Analysis of the integration of cohesive elements in regard to utilization of coarse mesh in laminated composite materials. Internat J Numer Methods Engrg 2014;99(8):566–86.

[46] Remmers JJ, Wells GN, Borst Rd. A solid-like shell element allowing for arbitrary delaminations. Internat J Numer Methods Engrg 2003;58(13):2013–40.

[47] Guiamatsia I, Ankersen JK, Davies GA, Iannucci L. Decohesion finite element with enriched basis functions for delamination. Compos Sci Technol 2009;69(15–16):2616–24. http://dx.doi.org/10.1016/j.compscitech.2009.08.002.

[48] Guiamatsia I, Davies GA, Ankersen JK, Iannucci L. A framework for cohesive element enrichment. Compos Struct 2010;92(2):454–9. http://dx.doi.org/10.1016/j.compstruct.2009.08.028.

[49] Främby J, Fagerström M, Brouzoulis J. Adaptive modelling of delamination initiation and propagation using an equivalent single-layer shell approach. Internat J Numer Methods Engrg 2017;112(8):882–908. http://dx.doi.org/10.1002/nme.5536.

[50] Guiamatsia I, Ankersen JK, Iannucci L. A study of mixed-mode composite delamination using enriched interface elements. Aeronaut J 2013;117(1195):959–67. http://dx.doi.org/10.1017/S0001924000008617.

[51] Russo R, Chen B. Overcoming the cohesive zone limit in composites delamination: modeling with slender structural elements and higher-order adaptive integration. Internat J Numer Methods Engrg 2020;121(24):5511–45. http://dx.doi.org/10.1002/nme.6497.

[52] Hansbo A, Hansbo P. A finite element method for the simulation of strong and weak discontinuities in solid mechanics. Comput Methods Appl Mech Engrg 2004;193(33–35):3523–40.

[53] van der Meer FP, Sluys LJ. A phantom node formulation with mixed mode cohesive law for splitting in laminates. Int J Fract 2009;158(2):107–24. http://dx.doi.org/10.1007/s10704-009-9344-5.

[54] Areias PM, Belytschko T. Non-linear analysis of shells with arbitrary evolving cracks using XFEM. Internat J Numer Methods Engrg 2005;62(3):384–415.

[55] Främby J, Fagerström M, Karlsson J. An adaptive shell element for explicit dynamic analysis of failure in laminated composites part 1: Adaptive kinematics and numerical implementation. Eng Fract Mech 2020;240:107288.

[56] Främby J, Fagerström M. An adaptive shell element for explicit dynamic analysis of failure in laminated composites part 2: Progressive failure and model validation. Eng Fract Mech 2021;244:107364. http://dx.doi.org/10.1016/j.engfracmech.2020.107364.

[57] Selvaraj J, Mukhopadhyay S, Kawashita LF, Hallett SR. Modelling delaminations using adaptive cohesive segments with rotations in dynamic explicit analysis. Eng Fract Mech 2021;245:107571. http://dx.doi.org/10.1016/j.engfracmech.2021.107571.

[58] Moslemi H, Khoei AR. 3D adaptive finite element modeling of non-planar curved crack growth using the weighted superconvergent patch recovery method. Eng Fract Mech 2009;76(11):1703–28. http://dx.doi.org/10.1016/j.engfracmech.2009.03.013.

[59] Khoei AR, Eghbalian M, Moslemi H, Azadi H. Crack growth modeling via 3D automatic adaptive mesh refinement based on modified-SPR technique. Appl Math Model 2013;37(1–2):357–83. http://dx.doi.org/10.1016/j.apm.2012.02.040.

[60] Kim J, Simone A, Duarte CA. Mesh refinement strategies without mapping of nonlinear solutions for the generalized and standard FEM analysis of 3-D cohesive fractures. Internat J Numer Methods Engrg 2017;109(2):235–58. http://dx.doi.org/10.1002/nme.5286.

[61] Chen BY, Pinho ST, De Carvalho NV, Baiz PM, Tay TE. A floating node method for the modelling of discontinuities in composites. Eng Fract Mech 2014;127:104–34. http://dx.doi.org/10.1016/j.engfracmech.2014.05.018.

[62] McElroy M. Use of an enriched shell finite element to simulate delamination-migration in a composite laminate. Compos Struct 2017;167:88–95. http://dx.doi.org/10.1016/j.compstruct.2017.01.057.

[63] Lu X, Chen BY, Tan VB, Tay TE. A separable cohesive element for modelling coupled failure in laminated composite materials. Composites A 2018;107(October 2017):387–98. http://dx.doi.org/10.1016/j.compositesa.2018.01.014.

[64] Lu X, Ridha M, Tan VB, Tay TE. Adaptive discrete-smeared crack (A-DiSC) model for multi-scale progressive damage in composites. Composites A 2019;125(January). http://dx.doi.org/10.1016/j.compositesa.2019.105513.

[65] Lu X, Chen BY, Tan VB, Tay TE. Adaptive floating node method for modelling cohesive fracture of composite materials. Eng Fract Mech 2018;194(March):240–61. http://dx.doi.org/10.1016/j.engfracmech.2018.03.011.

[66] Trabal GG, Bak BLV, Chen B, Lindgaard E. An adaptive floating node based formulation for the analysis of multiple delaminations under quasi-static loading. Composites A 2022;106846. http://dx.doi.org/10.1016/j.compositesa.2022.106846.

[67] Seshadri BR, Vieira De Carvalho N, Ratcliffe JG. Simulating the clamped tapered beam specimen under quasi-static and fatigue loading using floating node method. In: 2018 AIAA/ASCE/AHS/ASC structures, structural dynamics, and materials conference. 2018, p. 0971.

[68] De Carvalho NV, Krueger R. Modeling fatigue damage onset and progression in composites using an element-based virtual crack closure technique combined with the floating node method. Tech. rep., Hampton, Virginia: NASA; 2019.

[69] De Carvalho N, Mabson G, Krueger R, Deobald L. A new approach to model delamination growth in fatigue using the virtual crack closure technique without re-meshing. Eng Fract Mech 2019;222(April):106614. http://dx.doi.org/10.1016/j.engfracmech.2019.106614.

[70] Bak B, Turon A, Lindgaard E, Lund E. A benchmark study of simulation methods for high-cycle fatigue-driven delamination based on cohesive zone models. Compos Struct 2017;164:198–206. http://dx.doi.org/10.1016/j.compstruct.2016.11.081.

[71] Carreras L, Bak BL, Turon A, Renart J, Lindgaard E. Point-wise evaluation of the growth driving direction for arbitrarily shaped delamination fronts using cohesive elements. Eur J Mech A/Solids 2018;72(March):464–82. http://dx.doi.org/10.1016/j.euromechsol.2018.05.006.

[72] Carreras L, Lindgaard E, Renart J, Bak BL, Turon A. An evaluation of mode-decomposed energy release rates for arbitrarily shaped delamination fronts using cohesive elements. Comput Methods Appl Mech Engrg 2019;347:218–37. http://dx.doi.org/10.1016/j.cma.2018.12.027.

[73] Carreras L, Renart J, Turon A, Costa J, Bak B, Lindgaard E, Martin de la Escalera F, Essa Y. A benchmark test for validating 3D simulation methods for delamination growth under quasi-static and fatigue loading. Compos Struct 2019;210:932–41. http://dx.doi.org/10.1016/j.compstruct.2018.12.008.

[74] Carreras L, Renart J, Turon A, Costa J, Bak B, Lindgaard E, de la Escalera FM, Essa Y. Experimental data set from a benchmark test of delamination growth with varying crack growth rate and crack front shape under quasi-static and fatigue loading. Mendeley Data 2019;v1.

[75] Goutianos S, Srensen BF. Fracture resistance enhancement of layered structures by multiple cracks. Eng Fract Mech 2016;151:92–108. http://dx.doi.org/10.1016/j.engfracmech.2015.10.036.

[76] Benzeggagh M, Kenane M. Measurement of mixed-mode delamination fracture toughness of unidirectional glass/epoxy composites with mixed-mode bending apparatus. Compos Sci Technol 1996;56(4):439–49. http://dx.doi.org/10.1016/0266-3538(96)00005-X.

[77] Turon A, Camanho P, Costa J, Renart J. Accurate simulation of delamination growth under mixed-mode loading using cohesive elements: Definition of interlaminar strengths and elastic stiffness. Compos Struct 2010;92(8):1857–64. http://dx.doi.org/10.1016/j.compstruct.2010.01.012.

[78] Rice JR. Elastic fracture mechanics concepts for interfacial cracks. J Appl Mech 1988;55(1):98–103. http://dx.doi.org/10.1115/1.3173668.

[79] Blanco N, Gamstedt E, Asp L, Costa J. Mixed-mode delamination growth in carbon–fibre composite laminates under cyclic loading. Int J Solids Struct 2004;41(15):4219–35. http://dx.doi.org/10.1016/j.ijsolstr.2004.02.040.

[80] Juntti M, Asp LE, Olsson R. Assessment of evaluation methods for the mixed-mode bending test. J Compos Technol Res 1999;21(1):37–48.

[81] Sørensen BF, Jørgensen K, Jacobsen TK, Østergaard RC. DCB-Specimen loaded with uneven bending moments. Int J Fract 2006;141(1–2):163–76.

[82] Asp LE, Sjögren A, Greenhalgh ES. Delamination growth and thresholds in a carbon/epoxy composite under fatigue loading. J Compos Technol Res 2001;23(2):55–68.

[83] Alfano G, Crisfield M. Finite element interface models for the delamination analysis of laminated composites: mechanical and computational issues. Internat J Numer Methods Engrg 2001;50(7):1701–36.